Proceedings of ASME Turbo Expo 2020
Turbomachinery Technical Conference and Exposition
GT2020
June 22-26, 2020, London, England

TURBO-21-1025

AEROTHERMAL EFFECT OF CAVITY WELDING BEADS ON A TRANSONIC SQUEALER TIP

Joao Vieira*
joao.vieira@stcatz.ox.ac.uk
University of Oxford

John Coull
john.coull@eng.ox.ac.uk
University of Oxford

Peter Ireland
peter.ireland@eng.ox.ac.uk
University of Oxford

Eduardo Romero
eduardo.romero@rolls-royce.com
Rolls Royce PLC

ABSTRACT

High pressure turbine blade tips are critical for gas turbine performance and are sensitive to small geometric variations. For this reason, it is increasingly important for experiments and simulations to consider real geometry features. One commonly absent detail is the presence of welding beads on the cavity of the blade tip, which are an inherent by-product of the blade manufacturing process. This paper therefore investigates how such welds affect the Nusselt number, film cooling effectiveness and aerodynamic performance.

Measurements are performed on a linear cascade of high pressure turbine blades at engine realistic Mach and Reynolds numbers. Two cooled blade tip geometries were tested: a baseline squealer geometry without welding beads, and a case with representative welding beads added to the tip cavity. Combinations of two tip gaps and several coolant mass flow rates were analysed. Pressure sensitive paint was used to measure the adiabatic film cooling effectiveness on the tip, which is supplemented by heat transfer coefficient measurements obtained via infrared thermography. Drawing from all of this data, it is shown that the weld beads have a generally detrimental impact on thermal performance, but with local variations. Aerodynamic loss measured downstream of the cascade is shown to be largely insensitive to the weld beads.

1 INTRODUCTION

With the increase of turbine entry temperatures (TET) [1], shroudless High Pressure (HP) turbine blades are generally employed in preference to shrouded blades due to increased cooling difficulty, weight and limiting stresses caused by the presence of a shroud [2].

The necessity of tip gap arises from the need of having clearance between rotor blades and the casing. Overtip Leakage (OTL) is driven through the gap due to the active pressure differential present between pressure and suction sides of the blade [3]. The impact on engine performance is two-fold: first, the mixing of unturned flow with the mainstream generates around 1/4 to 1/3 of the total aerodynamic rotor loss [4 and 5]. Second, the tip is a region of substantial heat transfer with high surface area to volume ratio, which is inherently difficult to cool [6 and 7]. Thus, the TET is generally restricted by the need to minimize material damage and achieve sufficient engine life. This limitation in turn constrains engine thermal efficiency [3].

Many studies of tip geometries have been performed with the aim of achieving both greater cooling performance and lower losses. OTL was first characterized in incompressible flow conditions for a flat tip [8 and 9] with its general behavior being of separating at the pressure side edge of the tip and reattaching onto the tip surface downstream, causing a region of high Nusselt number (Nu). Between separation and reattachment exists a separation bubble, which has relatively low Nu.

The most common contemporary tip geometry is that of the squealer, consisting of a recessed cavity surrounded by rims. Such designs aim to improve efficiency by providing a double-wall seal against the OTL, however the design increases surface area and the intricate flow patterns in the squealer greatly augment heat transfer while complicating cooling hole placement. Experimental and computational studies have examined squealer tips in subsonic conditions [eg. 10 and 11]. Whilst Wheeler et al. [12] showed the importance of studying HP rotor tips in transonic environments, demonstrating that the OTL flow can be predominantly transonic with a strong coupling between shock structures and overtip boundary layer development. Other recent transonic studies on tip cooling include that of Naik et al. [13] on the effect of purge holes of squealer geometries on endwall temperatures at low turbulence intensities, while Arisi et al. [14] looked at the effect of Reynolds and Mach numbers on the flow features of a transonic ribbed squealer tip with 2 purge holes, concluding that higher tip leakage speeds negatively impact cavity cooling performance due to the increased strength of the cavity recirculation flow. Both studies were performed on linear cascade facilities.

1.1 REAL GEOMETRY EFFECTS

The majority of aerothermal studies on HP turbine blades have considered clean, idealized geometries. However, a number of studies into real geometry effects have demonstrated a substantial impact of these factors on performance. These effects can roughly be separated into three categories: manufacturing variability, geometrical details and in-service degradation.

Manufacturing variability refers to the unintended dissimilarities between components caused by the manufacturing processes. For example, a recent study in HP turbines by Lee et al. [15] examined the impact of the measured variability of a sample of 294 rotor blades on boundary layer properties and showed an average increase of 4.4% in the viscous loss with a spread of $\pm$ 8.3%.

For research and design purposes, it is common to exclude some geometrical details to allow easier manufacturing and/or evaluation. Examples of this are shroud cavities and vane-pack gaps on the platforms of stators [16]. Similarly, tips are tested with uninterrupted cavities and without rim abrasives [17].

In-service degradation considers the geometrical changes undergone by engine components during their lifetime. Bunker [18] studied the effect of surface roughness on vane heat transfer and showed that increasing roughness hastens transition and, thus, overall vane HTC. Bunker and Balley [19] looked at the effect of tip cavity depth and locally reducing Pressure Side (PS) and Suction Side (SS) rim height by 60%. Interestingly, trimming only the PS rim resulted in a localized 15% decrease of heat transfer on the cavity, while trimming both rims caused an overall increase in heat transfer, which was more pronounced downstream of the material loss region, demonstrating the complexity of tip thermal behaviour in the presence of realistic degradation patterns.

1.2 WELD BEADS

This paper investigates the aerothermal impact of weld beads on the performance of a transonic squealer tip. These beads are real geometry features that are inherent by-products of the manufacturing process. To provide core support and motivate adequate crystal growth, some parts of the tip cavity floor are left open during casting. For convenience, these openings are made to coincide with the internal serpentines, as exemplified in figure 1. At a later point, these cavities are welded shut, resulting on the creation of surface weld beads (blue components in figure 1). Dust holes are often drilled at the centre of these beads, as they are well aligned with the internal serpentines. These beads are usually left in place rather than machined away due to the extra costs involved and mechanical constraints.

The aim of the study is to experimentally investigate the aerothermal impact of weld beads on high pressure turbine blades. This investigation is conducted on a linear cascade rig, which enables higher resolution and fidelity of measurements than a rotating turbine, especially on complex geometries. However, the cascade does not reproduce the scrapping flow caused by the relative rotation of the casing. Saul et al. [17] have shown that, for a similar tip geometry, the scrapping flow only has a significant impact on the thermal properties of the cavity, whilst the rims are largely unaffected.

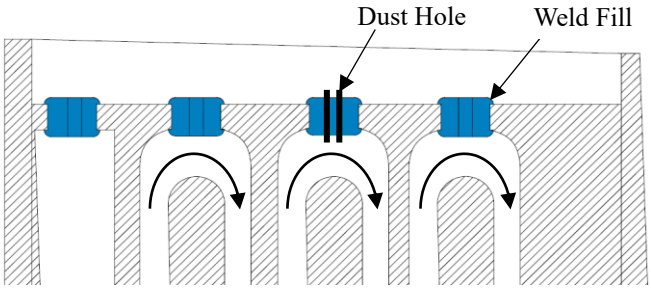

Figure 1: Schematic showing the placement of weld beads relative to the internal serpentines. Beads are shown in blue.

The effect of welds on Nusselt number, Film Cooling Effectiveness (FCE or η) and aerodynamic loss is studied at two tip clearances (0.65% span and 1.15% span) and different coolant mass flow rates ($\dot{m}_c$). A categorical approach to tip flow behaviours based on geometrical regions is employed to investigate the encountered phenomena.

2 EXPERIMENTAL METHODS

2.1 HIGH SPEED LINEAR CASCADE

The High Speed Linear Cascade is a blowdown wind tunnel with engine-realistic Mach and Reynold numbers, designed to evaluate the thermodynamic properties of HP turbine blade tips. This text will only offer a summarily description of the facility, which has been extensively described in [17, 20 and 21], of which [21] detailed the commissioning and specific operating conditions. General flow properties can be seen in table 1.

The test section (figure 2) consists of 5 blades, with the middle 3 having swappable roots and tips. Adjustments to the tip gap are achieved with an alterable height baseplate located underneath the test section. A turbulence mesh is located 5 axial chords (C_{ax}) upstream, generating a turbulence intensity of 8%, at a length scale of 0.3 C_{ax} [20].

As shown in figure 3, each of the middle blades contains 3 coolant plenums. The red, green and yellow demarcations highlight the Leading Edge (LE), middle and Trailing Edge (TE) plenums, respectively, as well as the cooling holes supplied by each of them. Either air or Oxygen-Free-Nitrogen can be fed to the system using 3 mass flow controllers, each in control of one plenum per blade. The split of the coolant between the blades is regulated by micrometer scaled needle valves. Every plenum is instrumented with static pressure tappings and thermocouples.

2.2 TEST GEOMETRIES

The baseline geometry (left-hand side of figure 4) is a squealer tip with open TE and slight overhangs on the TE section of the Pressure Side (PS) and Suction Side (SS) rims, similar to that studied by Saul in [17]. Near-tip cooling holes are present in the exterior of the squealer rim on both PS and SS.

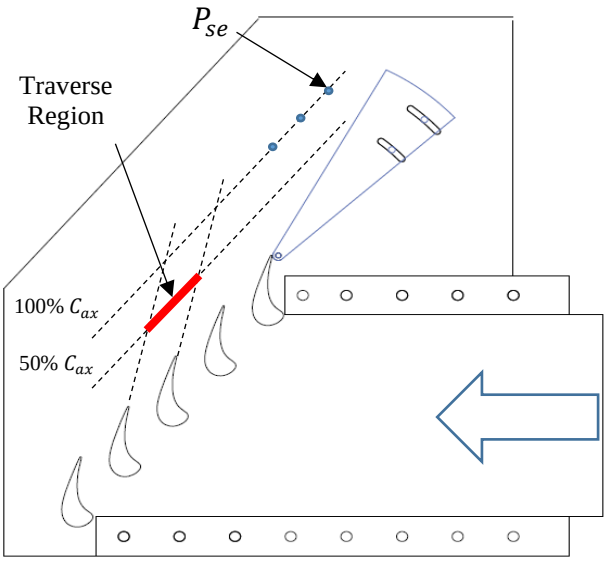

Figure 2: Test section schematic**.**

Inlet Mach Number	0.3
Exit Mach Number	0.99
Inlet Total Pressure	2.03 bars
Inlet Mass Flow	3.2 kg/s
Exit Reynolds Number	1.24×10^6

Table 1: Flow properties at cascade entry and exit.

Additionally there are 5 dust holes along the cavity camber line and 4 regular cooling holes near the inner surface of the SS rim. All cooling orifices are conventional cylindrical holes perpendicular to the cavity.

The tips were manufactured in both epoxy resin and Aluminium, with the former being used for Pressure Sensitive Paint (PSP) tests and the latter in IR and traverses. The difference between the tested baseline and the geometry in [17] is the presence of a larger number of cooling holes with smaller hole diameters, resulting in the same total coolant ejection area. To evaluate the effect of weld beads, 5 small inserts were attached to the cavity floor, as per the right-hand side of figure 4. For ease of reference, the beads will be numbered 1 to 5, from LE to TE. Geometrically, bead 1 is "D" shaped and is located at the cavity LE, beads 2 to 5 are roughly rectangular and are placed along the camber line, each with a dust hole along its length. All five beads have rounded edges. In terms of thickness, beads 1 to 4 are 1/3 of cavity height, whilst bead 5 is 1/4 of cavity height. As indicated in figure 4, the geometries will be referred hereafter as "clean" and "bead" geometries.

2.3 NUSSELT NUMBER

The impulse response model described by Oldfield in [22] is employed to measure Heat Transfer Coefficient (HTC), which utilises discrete deconvolution and Fourier transforms to derive filter impulse responses of linear, time intransient, systems with

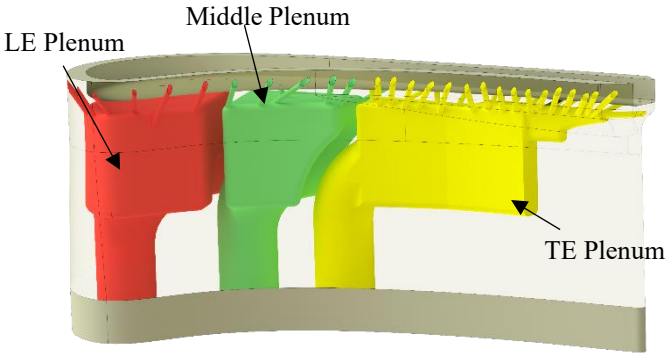

Figure 3: Color coded coolant plenums present in the test blade tips. Cooling holes are also color coded depending on the source plenum.

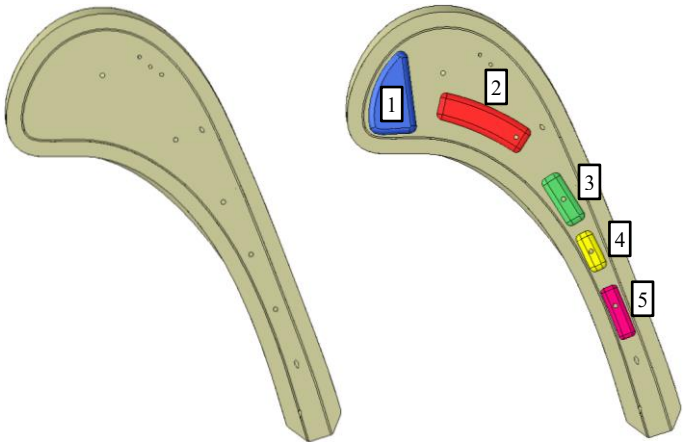

Figure 4: Test Geometries

steady initial values. This requires a 1D, semi-infinite assumption, reason why a low conduction epoxy resin tip painted matte black was used for these measurements.

$$\dot{q} = \mathrm{HTC}(\mathrm{T_{ad}} - T_w) \quad (1)$$

The heat flux ($\dot{q}$) is obtained from the temperature response of the surface. Then a regression analysis of the heat flux versus wall temperature is used to estimate the HTC and the adiabatic wall temperature (T_{ad}), as exemplified in figure 5. In this analysis, a linear function is fitted to the data at each pixel, with the slope of the line corresponding to the HTC and the extrapolated x-intercept being the T_{ad}.

Nusselt number is calculated as per equation (2), where k_{air} is the temperature-corrected local thermal conductivity of air:

$$Nu = \frac{HTC \cdot C_{ax}}{k_{air}} \quad (2)$$

A FLIR A655 IR camera is used to record the temperature response of the blade tip to an 18°C impulse caused by the facility heater mesh. Camera calibration is performed in-situ by comparing the obtained camera pixel-wise light intensities to the temperature readings of a thermocouple placed flush to the

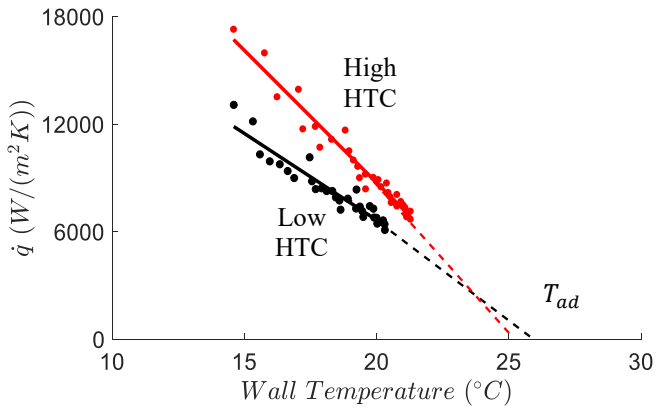

Figure 5: Regression analysis of heat flux versus wall temperature plots at two locations of the blade surface.

cavity floor.

Uncertainty of the impulse response method depends on the variance in tip material properties and individual uncertainties of: the greyscale IR camera reading, the in-situ calibration and the surface thermocouple. The measurement uncertainty for the configuration used in this publication was calculated to be approximately 7% by Saul et al [17].

An additional factor is that the semi-infinite assumption falters near the edges of the test piece, as the penetration depth of the surface temperature exceeds the available space. For the 0.9 seconds recording window used, the penetration depth is 0.2 mm, which consists roughly to 2 pixels at either side of the rims and at the back of the trailing edge. The impacted region is sufficiently small that this effect does not significantly influence the conclusions from Nusselt number measurements.

2.4 FILM COOLING EFFECTIVENESS

Pressure Sensitive Paint (PSP) is an optical technique to visualize pressure in which a surface is coated with organic luminophores mixed with a polymer binder [23]. Paint excitation is performed with 2 Intelligent LED Solutions 5W boards filtered to 410 ± 10 nm, as measured by a CCS200 Thorlabs spectrogram. Image acquisition is performed with a BigEye CCD camera filtered to 610 ± 10 nm. After steady flow conditions are reached for around 10 seconds, data are recorded at a frame size of 928 by 1452 pixels at 5 fps, with a total of 30 frames acquired per test condition, which are shake-corrected and averaged. A mass transfer analogy [24] is used to obtain FCE from the pressure readings, as per equation 3, where "C" is the partial concentration of O_2, the subscript "f" refers to film and "ref" to reference.

$$\eta \approx \frac{C_{air}-C_f}{C_{air}} \approx 1 - \frac{P_{O_2,f}/P_{O_2,ref}}{P_{O_2,air}/P_{O_2,ref}} \qquad (3)$$

The ratios $P_{O_2,f}/P_{O_2,ref}$ and $P_{O_2,air}/P_{O_2,ref}$ are obtained from two tests at the same conditions, except one uses Oxygen-Free-Nitrogen as the coolant fluid and the other uses air. Reference values ($P_{O_2,ref}$), used to compensate for the temperature dependency of the paint, are taken at the same average surface temperature as the previous tests, but without mainstream or coolant flow.

$$\frac{I_{ref}-I_{black}}{I-I_{black}} = f\left(\frac{P_{O_2}}{P_{O_2,ref}}\right) \qquad (4)$$

Calibration is necessary to link the measured intensities to the pressure ratios, as per the Stern-Volmer equation (4) [25]. This calibration is performed at a dedicated facility consisting of a controlled pressurization vessel, a thermal PID loop and an image acquisition system. The calibration sample was a 3 mm thick 15 by 15 mm Aluminum coupon, instrumented with an RTD at its center and painted together with the blade tips using the same layering procedure. Calibration range was 0.15 to 2 bars at the temperatures of 10°, 20° and 30°C. The obtained curve is shown in figure 6, which uses one reference per temperature condition to homogenize the data [26]. The two main sources of uncertainty in the PSP measurement are the camera color resolution (≈ 0.006% measurement error) and the paint pressure resolution (≈ 0.01 bar). Random camera noise is compensated by the aforementioned 30 frame averaging, while inherent bias and residual lighting are accounted for with an additional recording without any lights or flows (I_{black}). It can be demonstrated from equation 2 that the error related to the pressure resolution is inversely proportional to the difference between the pressure ratios $P_{O_2,f}/P_{O_2,ref}$ and $P_{O_2,air}/P_{O_2,ref}$, thus as η approaches 0, the error tends to become substantially larger. A perturbation analysis shows that for $\eta = 0.1$ the error is 0.06 in absolute effectiveness, while for $\eta = 0.5$ it decreases to 0.025.

2.5 AERODYNAMIC TRAVERSE

Aerodynamic loss measurements are performed with a four hole pressure probe located 0.5 C_{ax} downstream of the cascade exit (figure 2). Probe calibration was performed at the High Speed Tunnel at the Whittle Laboratory in the University of Cambridge. The pressure loss coefficient employed refers to the following: mid-span stagnation pressure at inlet measured by the upstream fixed pitot (P_{01}), exit stagnation pressure measured by the probe (P_{02}) and the static pressure one axial chord downstream measured by the wall static probe (P_{se}):

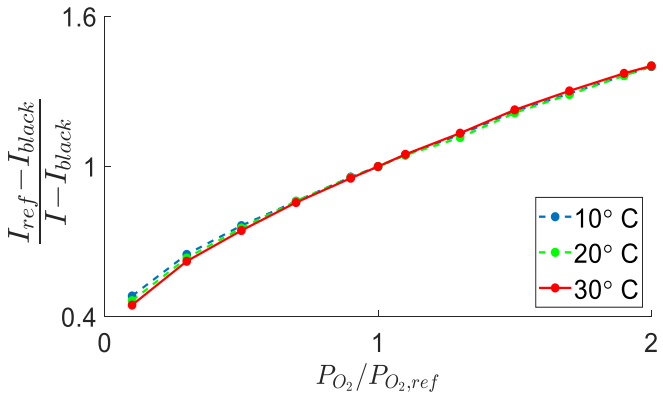

Figure 6: Pressure Sensitive Paint calibration curves.

$$C_{P0} = \frac{P_{01} - P_{02}}{P_{01} - P_{se}} \quad (5)$$

Uncertainty of the traverse measurements was evaluated with a perturbation analysis. At a 90% confidence interval, the uncertainty in the measurement of the yaw angle is ± 0.04 degrees, whilst for C_{P0} it is ± 0.001.

3 BASELINE PROPERTIES AND FLOW REGIONS

Figure 7 presents the baseline Nu (i-iii) and η (iv-vi) for the small tip gap at nominal $\dot{m}_c$. One can group the results into three main regions, each with its own flow behaviors and dependencies: **PS Rim**, **Cavity** and **SS Rim**.

Starting with FCE, the high effectiveness traces at the **PS Rim (iii)** are due to the near-tip holes present along the PS, from which coolant is jettisoned and directed against the rim by the OTL flow. Predictably, the rim coverage achieved by the ensuing films highly depends on the attachment behavior of the OTL over the PS rim.

In the **cavity (i)**, cooling holes generate high η over the downstream surface. Cooling performance of this region is largely dependent on the Blowing Ratio (BR) of the holes. At nominal conditions for this testing program, the BR is often sufficiently large to cause the films to lift-off from the cavity floor, resulting in diminished η downstream.

The **SS rim (ii)** is not directly cooled, but rather receives accumulated coolant carried over by the OTL flow from the PS near-tip holes and any coolant that lifts-off from the cavity holes. This behavior can be interpreted as the global cooling of the geometry, with more coolant being added gradually from upstream to downstream via the natural motion of the flow. A similar effect can also be seen along the cavity floor, with the gradual increase in η from LE to TE due to the accumulation of coolant on that surface.

Moving on to Nu, flow behavior at the **PS rim (vi)** is very similar to that around a flat tip, as described by Yamamoto and Moore [8 and 9], where the OTL rolls over the PS edge of the rim due to the strong active pressure gradient, causing the formation of a separation bubble, inside of which the Nu is low. After the bubble, the flow reattaches to the rim, where mixing generates high Nu [9 and 10]. These features are more readily observed in the large tip gap results, where the separation bubble is larger and thus there is a more sizeable region of low Nu (compare cases in figure 8 (a) to those in 8 (c)). This behavior, its dependency on tip gap and how it varies with the introduction of weld beads are discussed in detail in section 4.2.

Cavity Nu (iv) is mostly dominated by two effects, one related to coolant flow and the other independent of it. The coolant flow dependency is the Nu magnification caused by the mixing of the coolant jets and the cavity flow, locally raising Nu downstream of the cooling holes, notably this effect is responsible for the high Nu region in the inner SS of the cavity. The other effect is the impingement of flow onto the cavity floor

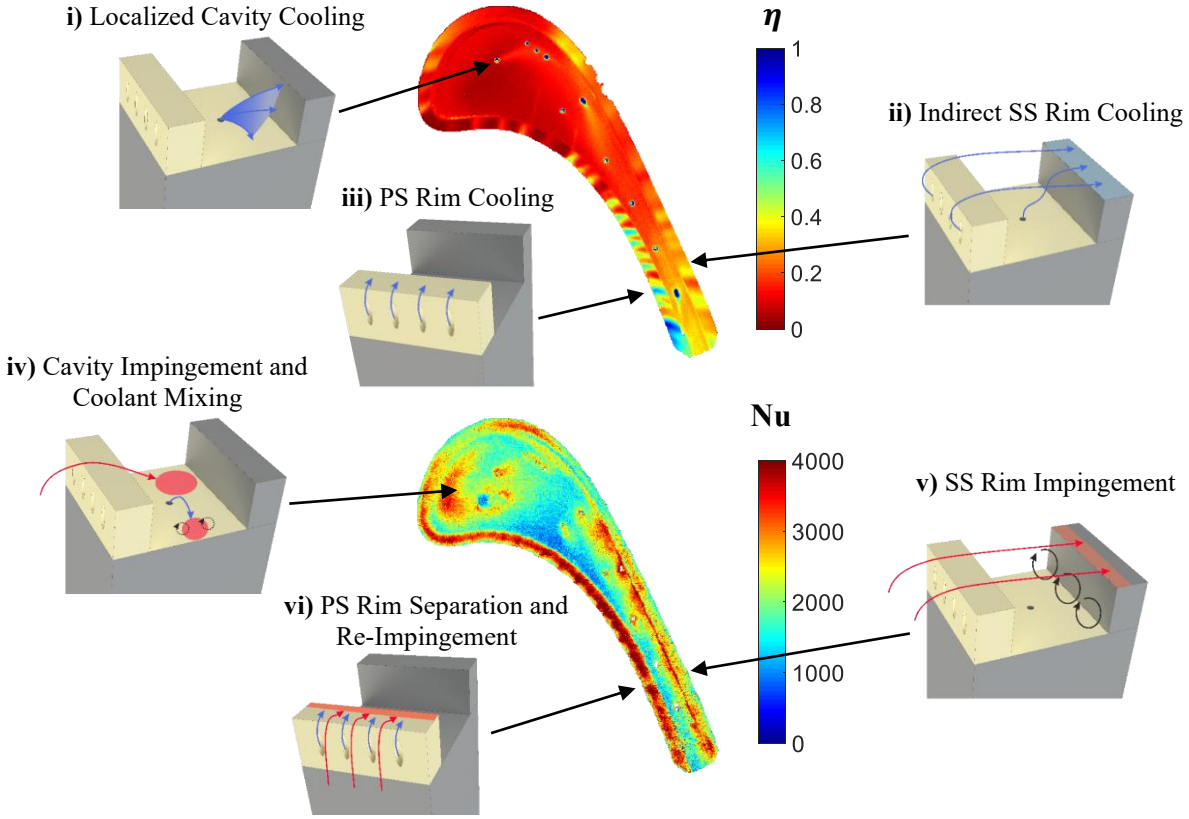

Figure 7: Baseline Nusselt number and film cooling effectiveness surface contours at small tip gap (0.65% g/S) and nominal coolant flow. Insert diagrams illustrate key heat transfer and cooling effectiveness mechanisms.

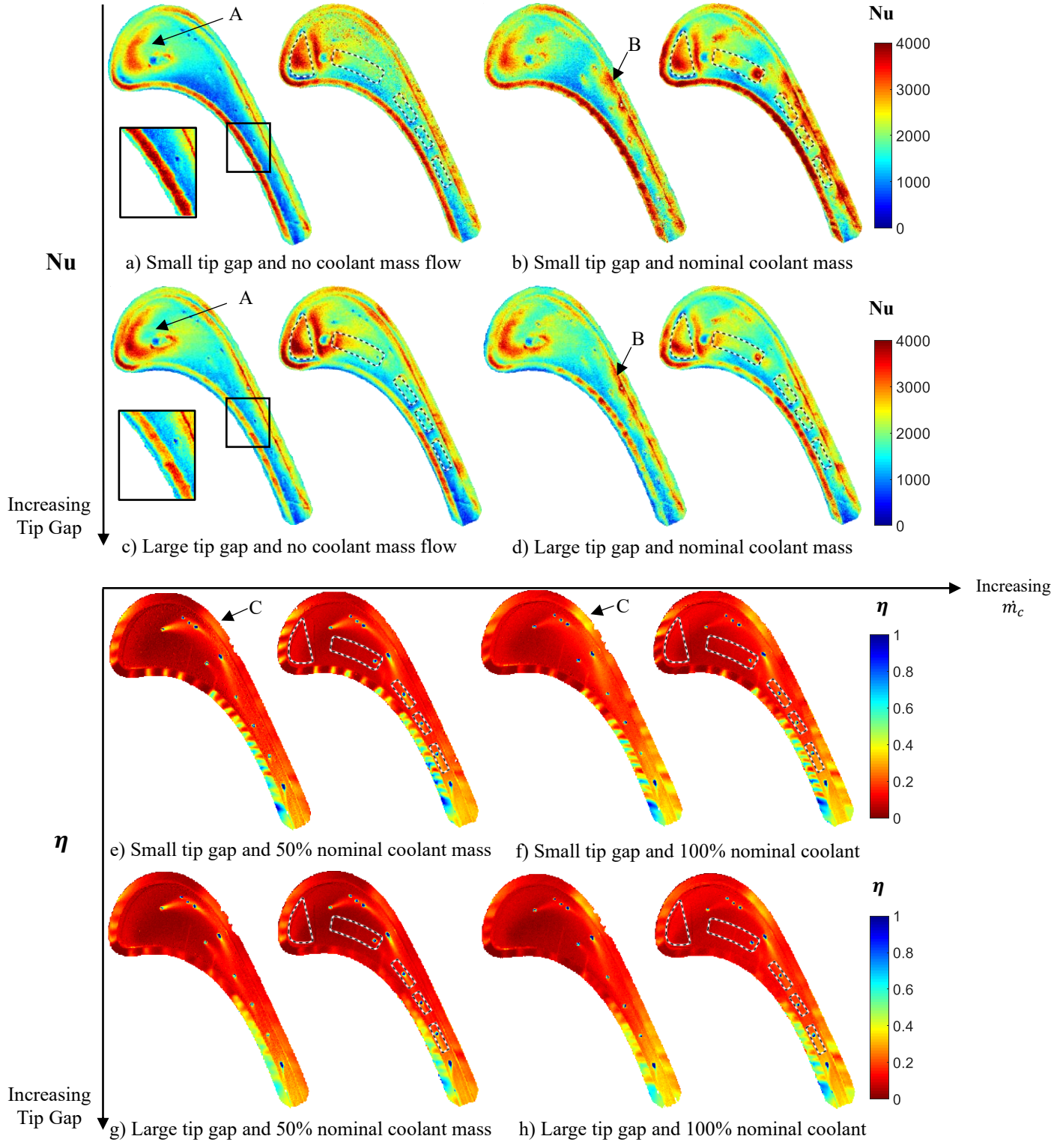

Figure 8: Experimental Nu and η results for the tested geometries. Cases are paired up with the clean geometry on the left and the bead geometry on the right. The b) and d) Nusselt number results correspond to the cases with the identifiers f) and h) in the η results.

downstream of the PS, which generates regions of high Nu, such as the hotspot near the LE region of the cavity.

Further aft. on the blade, the cavity is narrower and the flow directly impinges onto the **SS rim (v)**, this causes a low Nu region on the PS of the cavity and Nu magnification at the SS rim. Towards the LE, the observed regions of high Nu are portions of the rim that are directly impinged by the cavity flow. Additionally, the cavity vortex causes Nu enhancement in the region [26], some of which affects the SS rim.

4 IMPACT OF WELD BEADS

This section examines the impact of weld beads on the clean geometry results, which is better explained by analyzing the local percentage variation from mean (%Δμ) between clean and bead geometries as per the following equation:

$$\%\Delta\mu = \frac{case\_beads - case\_clean}{area\_average(case\_clean)} \times 100 \qquad (6)$$

4.1 FILM COOLING EFFECTIVENESS

Figure 9 shows the change in FCE for two cases: b) demonstrates the alterations caused by adding the weld beads to the baseline η shown in figure 7, while a) shows the alterations on a test with half the amount of coolant, useful for comparison purposes.

In the η contours, most cooling holes are the origin of one red and one blue trace. This pattern represents a change in trajectory of the coolant; i.e. beads cause coolant to move away from the red regions and towards the blue region. Furthermore, comparing the relative sizes of the red and blue traces demonstrates the net effect on FCE.

PS Rim: The most significant FCE alteration is at the PS rim, where the presence of weld beads alters the OTL flow, slightly shifting the coolant stream and causing the alternating low and high η pattern. There is also a slight overall η increase. These effects are largely driven by the blockage in the cavity, where the weld beads act to reduce the cavity pressure. Further discussion on this behavior will be provided in the next section.

Cavity: The introduction of the beads alters the streamlines formed on the blade cavity. This impact becomes evident when looking at the jets produced by the cavity cooling holes. Since these orifices are perpendicular to the surface, the ensuing jets naturally follow cavity streamlines.

At hole A, the cavity flow changed from being essentially parallel to the SS rim to pointing more towards the inside of the cavity. It can also be observed that the blue trace originating from the hole covers a larger area than the red trace, suggesting an overall improvement in jet efficiency. The sensitivity to coolant mass flow (Section 5.2) evidenced that the cavity holes are prone to reductions in η due to jet lift-off at high $\dot{m}_c$. Thus, the improved FCE at hole A is driven by faster cavity flow in the presence of beads, resulting in a decrease of hole BR and an improvement of jet coverage. A similar behavior is seen at hole B, which also points more towards the PS rim. The reorientation of the jets at these two holes strongly suggests that the beads strengthened the cavity vortex, which flows from the SS to PS

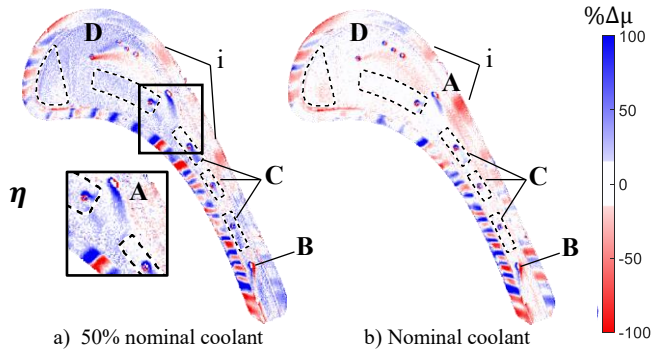

Figure 9: Percentage FCE variation from mean caused by the introduction of weld beads for two test conditions at small tip gap. Case a) at 50% coolant, whilst case b) is nominally cooled.

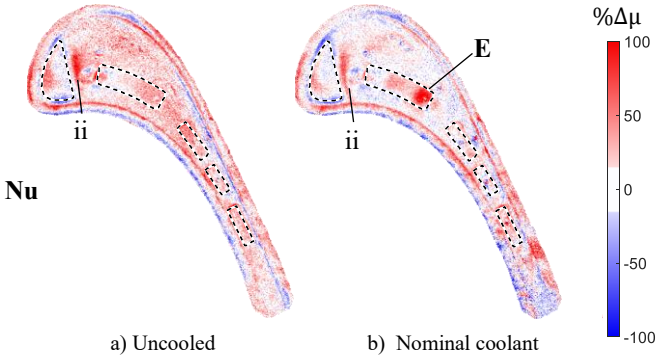

Figure 10: Percentage Nu variation from mean caused by the introduction of weld beads for two test conditions at small tip gap. Case a) is uncooled, whilst case b) is nominally cooled.

direction at the cavity floor [26].

Holes C – located in beads 3, 4 and 5 – show an η increase in most test conditions when compared to the clean geometry, with the blue streams extending over the bead surface and stopping abruptly at the edges of the beads, which is more readily visible in case a) of figure 9. This suggests that the extra blockage causes the cavity flow to accelerate over the welds, improving the BR of the holes.

Conversely, holes D undergo an η penalty, which is likely due to slower cavity flow in the region caused by its proximity to the expanded LE Nu hotspot (ii in figure 10). For this reason, the velocity at D is lower than in the clean geometry, causing an increase in hole BR and, consequentially, lower η.

SS Rim: Expectedly, the indirect nature of the SS rim cooling will cause the changes seen at this surface to depend on the aforementioned changes to the PS rim and cavity. Firstly, the lift-off reduction observed at the cavity holes and the deflection of some jets towards the PS negatively impacts the SS rim, as more coolant remains attached to the cavity floor rather than passing over the SS Rim. This is evident downstream of hole A and at the first hole C, at locations (i). Holes D are an exception, as the progression of their jets is intended to directly cool the SS rim via impingement, however the increased jet lift-off will instead redirect the coolant away from the rim and into the OTL,

decreasing η.

Secondly, the improved coolant attachment at the PS rim due to the reduced static pressure increases the amount of coolant available at rim height. This benefits the SS rim, especially towards the TE, where the cavity is narrower and, thus, the coolant leaving the PS rim has less space to diffuse into the OTL flow, causing slight η improvements in the TE portion of the rim.

4.2 NUSSELT NUMBER

The introduction of weld beads significantly changes the Nu distribution, as seen in cases a) and b) of figure 10. As in the previous section, b) corresponds to the changes caused by the beads to the baseline from figure 7, whilst a) is an uncooled case used to ascertain the dependency of the observed behaviors on the coolant flow.

PS Rim: In both cases a) and b) of figure 10, it is observed that the Nu at the PS rim increases with the introduction of beads. The Nu and η changes observed can be explained by examining the influence of the beads on the static pressure of the tip. Figure 11 presents the static pressure from the PSP measurements for both the small and large tip gaps at nominal coolant, with and without beads. The bead geometry has generally lower static pressure due to the increased blockage caused by the welds, which locally decrease cavity depth, effect that is more relevant at lower tip gap. Consequentially, the Mach number of the OTL flow over the PS rim will be higher, causing the separation bubble to shrink in the bead geometry.

At lower tip gap – a) and b) in figures 11 and 12 – the bubble is already relatively small on the clean geometry, thus, even though the change in static pressure is more pronounced, it has diminishing returns on the size of the reattachment region (compare cases (a) and (b) of figure 8). On the other hand, at higher tip gap – c) and d) in figures 11 and 12 – the bubble is much larger, thusly being more affected by the static pressure reduction, significantly increasing the size of the reattachment region.

Hence, the reduced overall static pressure causes an increase in PS rim Nu, which is more significant at larger tip gap. Likewise, η is also positively affected by the larger reattachment region.

Cavity: In general terms, the beads increase the overall cavity Nu, especially in the immediately adjacent areas. This is expected, as the beads act as functional turbulators, altering the flow path with additional separations and reattachments and thus increasing the mixing and turbulence, which are well known causes of high HTC [27]. The uncooled case a) in figure 10 makes this effect especially apparent.

The largest change occurs at the LE hotspot (ii in figure 10), which expands considerably, this is evidence of the enlargement of the LE impingement region, with bead 1 forcing the flow to re-impinge onto the cavity downstream of its rounded edge.

In the nominally cooled case, b) in figure 10, a new hotspot is present at position E, which coincides with the location of the cooling hole in bead 2. Referring back to figure 4, note that bead 2 is the only one with a cooling hole

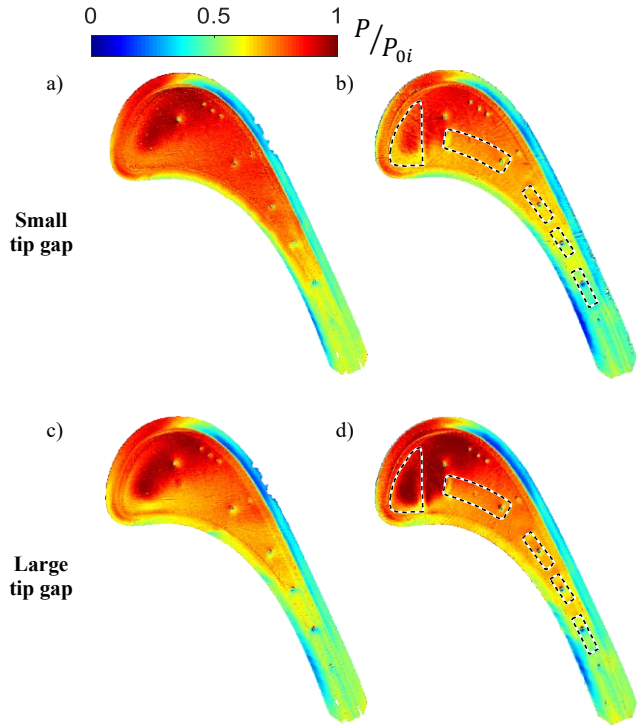

Figure 11: Static pressure contours at small and large tip gaps. Clean geometry on the left and bead geometry on the right.

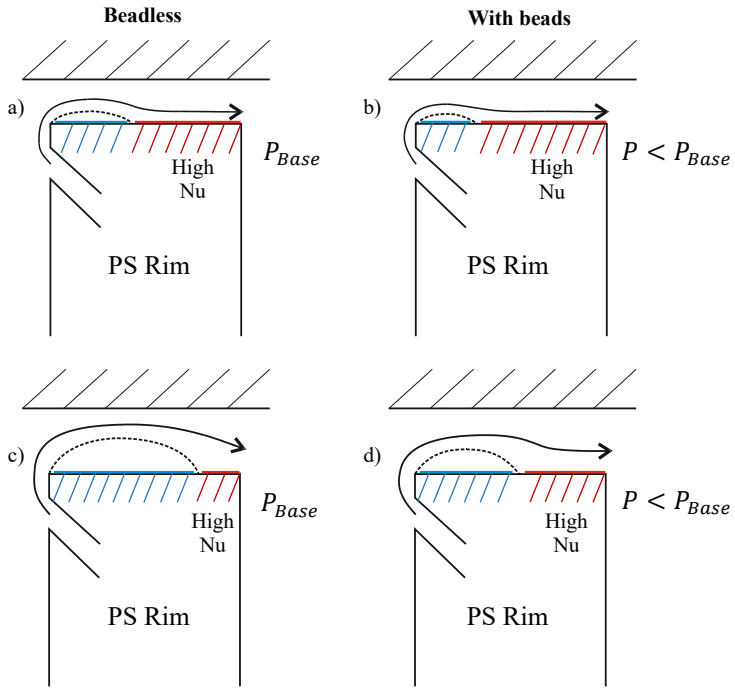

Figure 12: Schematic representation of the separation bubble and reattachment regions. Images coincide with those from figure 11.

close to its back edge, this coincides with where the cavity flow following the shape of the bead would begin redirecting back into the cavity floor. However, the presence of coolant could disrupt this, causing the flow to separate and mix around the curvature change instead of remaining attached, greatly increasing Nu. Beads 3, 4 and 5 have their dust holes at a sufficient distance from their respective back edges to not be affected by this, thus, the Nu over those beads is similar to that of the clean geometries.

SS Rim: As was discussed, the greater η adhesion to the PS rim in the presence of beads positively impacts the coolant propagation downstream, increasing the overall η at the TE portion of the SS rim. In turn, this increases near-surface mixing and thus, the Nu in the region. The uncooled cases at both tip gap clearances have essentially the same Nu distribution at the SS rim, corroborating that the changes seen here are mostly dependent on the coolant flows. Another factor is the superior jet attachment to the cavity in the case with welds, which generates more near-surface mixing, resulting in some Nu rise on the SS rim in regions downstream of the cooling holes.

5 NUSSELT NUMBER AND FILM EFFECTIVENESS SENSITIVITY

The sensitivity of the baseline conditions to tip gap and coolant mass flow is examined in this section. Figure 13 presents the Nu and η area averages for the baseline and bead geometries at nominal $\dot{m}_c$ and both tip gaps, individual cases are shown in figure 8.

5.1 SENSITIVITY TO TIP CLEARANCE

PS Rim: Comparison of the clean geometry low and large tip gap cases in figure 13, shows that the overall PS rim Nu and η are highly dependent on tip gap, where it is seen that both attain lower values at larger clearance. This behavior is caused by the expected enlargement of the separation bubble, which contracts the high Nu reattachment region and compromises film attachment to the rim, as exemplified in sketches a) and c) of figure 12 and observed by comparing the PS rims of a) and c), as well as, e) and g) in figure 8.

The weld bead impact on Nu and η is similar at both clearances, but the changes are more pronounced at high clearance, with a greater enlargement of the reattachment region, as depicted in c) and d) of figure 12. This results in a higher percentage increase of Nu and η between the clean and bead geometries at the large tip gap.

Cavity: Increasing tip clearance decreases cavity Nu, with the most notable difference being the high Nu region near the SS rim (B in figure 8). Additionally, similar to what was observed by Saul et al [17], the LE hotspot (A) tends to increase with clearance in the uncooled cases, but is inhibited by the blockage generated by the coolant flow from the LE near-tip cooling holes, thus not being as relevant in the presence of coolant.

Only small η changes are seen overall. It is worth noting

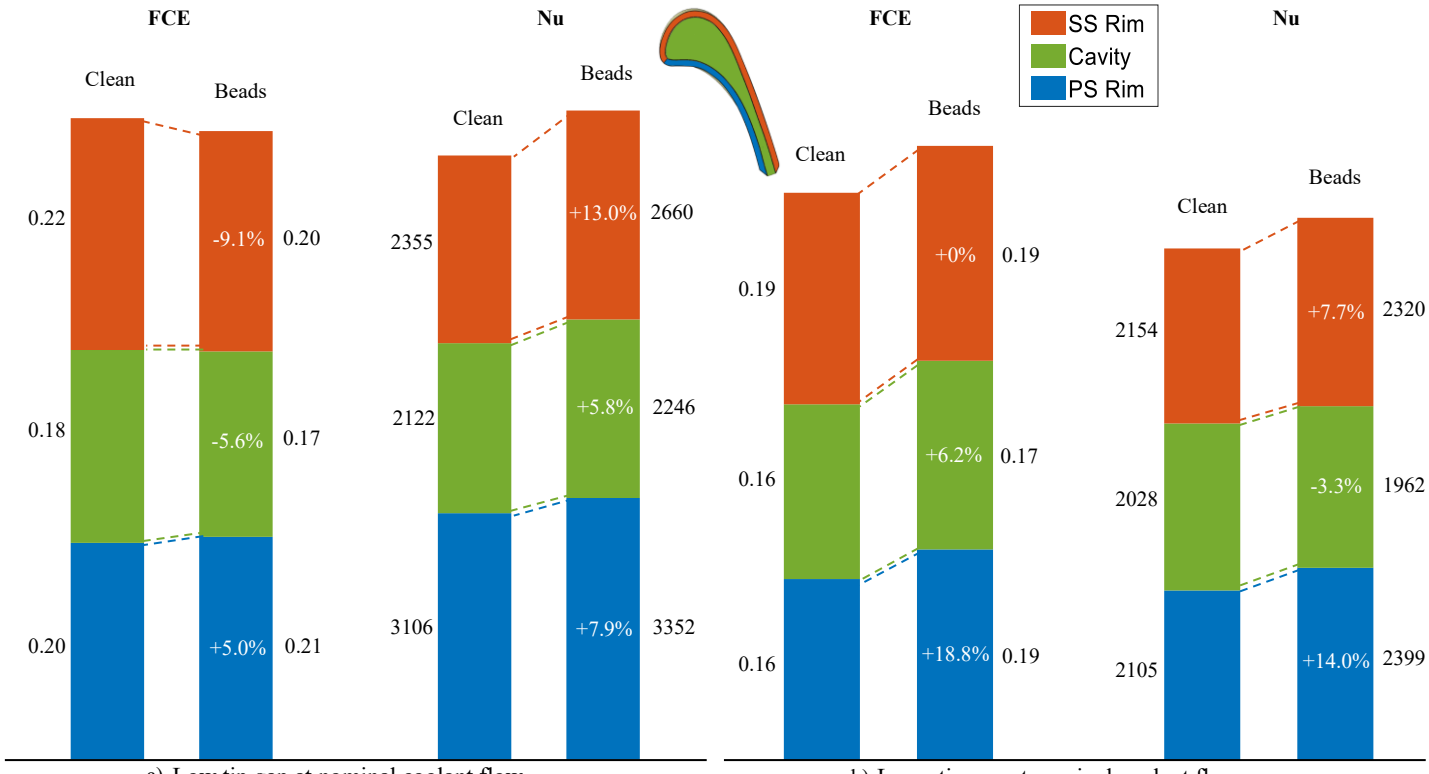

a) Low tip gap at nominal coolant flow

b) Large tip gap at nominal coolant flow

Figure 13: FCE and Nu area averages for the clean and bead geometries at small and large tip gaps.

here that η levels are generally low over most of the cavity, as such the average error is relatively large. Comparison of the high η regions in cases e) to h) of figure 8 does not reveal any significant η alterations caused by the tip gap increase.

SS Rim: Again, SS Rim behavior is intrinsically linked to the PS Rim and cavity due it being indirectly cooled by the holes originating from these two regions. As detailed in section 4.2, at constant coolant mass flow, the increase of Nu and η at the PS rim weakly correlate to an increase of the same variables over the SS rim, especially towards the TE, due to the narrow cavity. This factor is reflected on the impact of the welds at larger tip gap not being as detrimental to the SS Rim as in the low tip gap case – a) in figure 13 – due to the improvements in η at the PS rim, which propagate to the SS, counteracting the negative effect of the enhanced jet adhesion to the cavity floor.

Overall: In general terms, the weld beads caused Nu to increase in most conditions. Total area averages can be seen in figure 14, where it is shown that cases with beads produced 11.9% and 6.2% more Nu at small and large tip gaps, respectively. Trends in FCE are less directly apparent. At nominal coolant, the beads were beneficial at large tip gap, but were mostly indifferent at low tip gap. However, it is paramount to understand that the local η differences between the geometries with and without beads can be substantial, as was seen in section 4.1.

5.2 SENSITIVITY TO COOLANT MASS FLOW

Comparison of f) and e), as well as, h) and g) in figure 8 shows that a decrease in $\dot{m}_c$ causes localized increments in PS rim and cavity FCE, with most cooling holes showing higher η jets. This evidences that the decrease in coolant flow has caused the jets to better attach to the surface, which in turn shows that BR reductions are beneficial for the coolant attachment at these testing conditions. In contrast, the SS rim becomes considerably worse, due to the overall decrease in the amount of coolant in the system.

Expectedly, as seen in figure 14, the 50% $\dot{m}_c$ cases have lower overall Nu and η due to the reduced amount of coolant in the system and consequent reduction in flow mixing. An exception is the large tip gap Nu cases, where the aforementioned coolant blanketing effect at the PS rim is sufficient to counterbalance the extra Nu generated by the mixing at 100% $\dot{m}_c$.

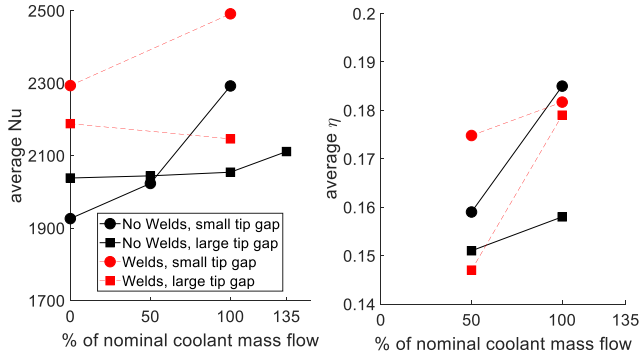

Figure 14: Spatial averages for all tested conditions. Clean cases in black and bead cases in red. Plot on the left is Nu and plot on the right is FCE.

Figure 15 summarizes the alterations caused by the beads on each geometrical region of the studied transonic squealer tip, explaining the produced impact on Nu and η, as well as the mechanisms that generate them. As can be seen, these relatively small geometrical alterations caused a plethora of significant changes, with the most relevant being the reduction of static pressure caused by the additional blockage, which resulted in higher Mach numbers at the PS rim and cavity.

6 AERODYNAMIC LOSS

Pitch-wise spatial-averaged loss coefficient (equation 5) and yaw angle contours measured 0.5 C_{ax} downstream of the TE are shown in figure 16 at 0.65% and 1.15% g/S tip gaps for both the clean and bead geometries without coolant flow. The overall behavior is consistent across all 4 test conditions. A tip leakage loss core is evident at around 0.9 to 0.95 of span. This flow, consisting mostly of OTL, is underturned relative to the midspan, as indicated in figure 16. At larger tip gap, more OTL is present making these effects more pronounced.

Direct comparison of the cases with and without beads shows no significant alterations, suggesting that the tested bead configuration did not have a significant impact on the downstream aerodynamics. Similar results were found for cooled tests, omitted for brevity. The aerodynamic impact of the weld beads in a real engine is likely to be more significant due to the stronger cavity vortex induced by the relative casing motions [17], not present in this cascade.

7 CONCLUSIONS

The impact of weld beads on a transonic squealer blade tip geometry was explored at a high speed linear cascade with representative Mach and Reynolds numbers. The introduction of the beads resulted in significant alterations to the heat transfer of the blade tip. This impact can be split into two key factors: turbulator effect and localized cavity blockage.

- The beads act as turbulators, increasing flow mixing and turbulence of the cavity flow.
  - Augments Nusselt number (Nu) in the vicinity of the beads and in the downstream flow direction.
  - Causes the enlargement of the LE Nu hotspot and generated a new hotspot along the camber line of the tip.
  - This led to an overall Nu increase of approximately 8% over the baseline geometry.
- The blockage from the beads reduces the effective cavity depth, decreasing the static pressure and increasing the velocity in the cavity.
  - This effect increases the pressure ratio over the PS rim, causing higher Mach numbers and leading to an earlier reattachment on the rim. This increases Nu in the region and brings more coolant in contact with the surface, also increasing film cooling effectiveness (η).

Feature	FCE	Nu	Mechanism
Pressure side and LE rims 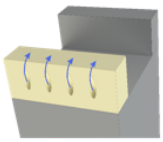	• Movement of films causes redistribution of coolant • Slighly higher average	• Overall higher average	Lower cavity pressure due to blockage of beads (figures 10 and 11): • Higher pressure ratio over PS rim • Larger reattachment region • More pronounced at higher tip gap
Cavity, near beads • Uncooled 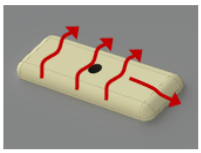	———	• Expand LE hotspot • Separation and reattachment enhancement around the beads	• Beads act as effective turbulators • Increased flow mixing and turbulence
• Cooled 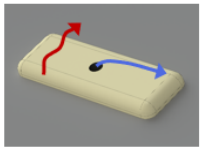	Changes to cooling holes (figure 8): • Redirect and enhance holes A and B • Improve attachment of holes C • Increased lift-off at holes D	• New hotspot at hole E (figure 9) • Some enhancement downstream	• Increased cavity velocity due to added blockage, effectively decreasing cavity depth • More favorable hole BR causes coolant flow to remain attached to bead surface • Expansion of the LE hotspot negatively affects the LE holes
SS Rims 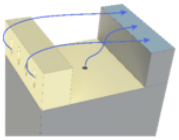	• Lower downstream of cooling holes (i in figure 8) • Slight improvements near TE	• Higher downstream of the beads • Higher in regions of improved FCE towards the TE	• FCE is negatively impacted by the enhanced adhesion of the jets to the cavity • Improved coolant attachment at the PS rim propagates downstream causing more near-surface mixing • Influenced by the turbulator effect

Figure 15: Summary of the impact of weld beads on Nu and η.

- The faster cavity speeds reduce the BR of the cooling holes, leading to larger values of η on the cavity floor.
- The improved attachment of the coolant jets to the cavity floor is detrimental to the η of the SS rim, as more coolant leaves the blade through the TE opening rather than being redirected by the OTL flow.
- Likewise, the improved jet attachment causes more near-surface mixing, locally increasing cavity and SS Rim Nu.

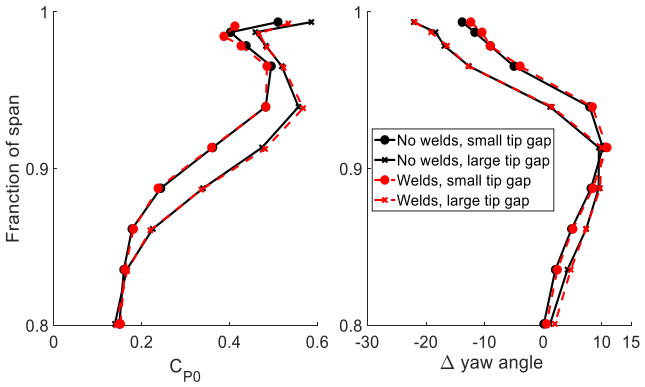

Figure 16: Pitch-wise spatial-averaged loss coefficient (C_{P0}) and yaw angle at 0.65% and 1.15% tip gaps. In the yaw angle plot, the x-axis is the difference between the measured and the blade exit angle, negative values represent underturned flow, while positive values represent overturned flow.

- The aerodynamic performance of the cascade was not significantly affected by the presence of the beads.

Based on these results, it will be beneficial for thermal performance to minimise the protrusion of weld beads above the cavity floor.

8 ACKNOWLEDGEMENTS

This project was funded by the Engineering and Physical Sciences Research Council, and by the Innovate UK iCore project with funds from Rolls-Royce plc. and the Aerospace Technology Institute. In addition, the authors would like to thank: Andrew Saul for his assistance with the experimental rig; Andrew Melzer for his assistance in calibrating the four hole probe; Fred Goenaga, Haidong Li and Anton Rawlinson of Rolls-Royce for their technical assistance; and the technicians and staff at the Oxford Thermofluids Institute.

9 NOMENCLATURE

Abbreviations

BR	Blowing Ratio
FCE	Film Cooling Effectiveness (η)
HP	High Pressure
HTC	Heat Transfer Coefficient
LE	Leading Edge
OTL	Overtip Leakage
PS	Pressure Side
SS	Suction Side
TE	Trailing Edge

TET	Turbine Entry Temperature

Symbols

C_{ax}	Axial chord (scaled, 49 mm)
$\dot{m}_c$	Coolant mass flow rate
I	Intensity
P	Pressure
T	Temperature
Nu	Nusselt number

Subscripts

ad	Adiabatic
c	Coolant
f	Film
i	Initial conditions
∞	Mainstream flow conditions
o	Stagnation or total
w	Wall

10 REFERENCES

[1] Dutta, S., Ekkad, S., and Han, J. 2000. Gas Turbine Heat Transfer and Cooling Technology. CRC Press, Florida.

[2] Harvey, N. 2004. von Karman Lecture Series: Turbine blade tip design and tip clearance treatment.

[3] Dixon, S. and Hall, C. 2016. Fluid Mechanics and Thermodynamics of Turbomachinery. 7th Edition. Elsevier, Florida.

[4] Boyle, R., Haas, J. and Katsanis, T. 1984. Comparison between Measured Turbine Stage Performance and the Predicted Performance using Quasi-3D Flow and Boundary Layer Analyses. JO - NASA Technical Memorandum.

[5] Denton, J. D. 1993. Loss Mechanisms in Turbomachines. J. Turbomach, 115(4): 621-656.

[6] Dunn, M.G. and Haldeman, W. 2000. Time-averaged heat flux for a recessed tip, lip, and platform of a transonic turbine blade. J. Turbomach 122(4): 692-698

[7] Glezer, B. 2004. von Karman Lecture Series: Turbine Blade Tip Design and Tip Clearance Treatment. VKI LS 2004-02, Turbine blade tip design and tip clearance treatment.

[8] Yamamoto, A., 1988. Interaction Mechanisms Between Tip Leakage Flow and the Passage Vortex in a Linear Turbine Rotor Cascade. J. Turbomach, 110(3): 329-338

[9] Moore, J., and Tilton, J. S., 1988. Tip Leakage Flowin a Linear Turbine Cascade. J. Turbomach, 110(1): 18-26

[10] Azad, G. S., Han, J.-C., Bunker, R. S., and Lee, C. P., 2002. Effect of Squealer Geometry Arrangement on a Gas Turbine Blade Tip Heat Transfer. J. Heat Transfer, 124(3): 452–459.

[11] Kwak, J. S., Ahn, J., Han, J.-C., Lee, C. P., Bunker, R. S., Boyle, R., and Gaugler, R., 2003. Heat Transfer Coefficients on the Squealer Tip and Near-Tip Regions of a Gas Turbine Blade with Single or Double Squealer. J. Turbomach, 125(4): 778–787.

[12] Wheeler, S., Atkins, R., and He, L., 2011. Turbine Blade Tip Heat Transfer in Low Speed and High Speed Flows. J. Turbomach, 133(4): 041025

[13] Naik, S., Georgakis, C., Hofer, T., and Lengani, D. 2011. Heat Transfer and Film Cooling of Blade Tips and Endwalls. ASME. J. Turbomach. July 2012; 134(4): 041004.

[14] Arisi, A., Phillips, J., Ng, W. F., Xue, S., Moon, H. K., and Zhang, L. 2016. An Experimental and Numerical Study on the Aerothermal Characteristics of a Ribbed Transonic Squealer-Tip Turbine Blade With Purge Flow. J. Turbomach October 2016; 138(10): 101007.

[15] Lee, W., Dawes, W., Goenaga, F. and Coull, J. 2018. The Impact of Manufacturing Variability on High Pressure Turbine Profile Loss. 2018 AIAA Aerospace Sciences Meeting. https://doi.org/10.2514/6.2018-2121

[16] Taylor, D. and Longley, J. 2018. Effects of Stator Platform Geometry Features on Blade Row Performance. GPPS Montreal 2018. 10.5281

[17] Saul A., Ireland P., Coull J., Wong H., Li H., and Romero E. 2018. An Experimental Investigation of Adiabatic Film Cooling Effectiveness and Heat Transfer Coefficient on a Transonic Squealer Tip. J. Turbomach. 141(9): 091005

[18] Bunker, R. 1997. Separate and Combined Effects of Surface Roughness and Turbulence Intensity on Vane Heat Transfer. Proceedings of the ASME 1997 International Gas Turbine and Aeroengine Congress and Exhibition. June 2–5, 1997. V003T09A022. ASME.

[19] Bunker, R. and Balley, J. 2001. Effect of Squealer Cavity Depth and Oxidation on Turbine Blade Tip Heat Transfer. Proceedings of the ASME Turbo Expo 2001: Power for Land, Sea, and Air. June 4–7, 2001. V003T01A038. ASME.

[20] Zhang Q., O'Dowd D., He L., Wheeler A., Ligrani P. and Cheong B. 2011. Overtip Shock Wave Structure and Its Impact on Turbine Blade Tip Heat Transfer. J. Turbomach. 133(4): 041001

[21] O'Dowd D., Zhang Q., He L., Ligrani P. and Friedrichs S. 2011. Comparison of Heat Transfer Measurement Techniques on a Transonic Turbine Blade Tip. ASME. J. Turbomach. 133(2): 021028.

[22] Oldfield, L., 2008. Impulse Response Processing of Transient Heat Transfer Gauge Signals. J. Turbomach, 130(2), Mar., pp. 021023–021023–9.

[23] Foss, J., Tropea, C., and Yarin, A. 2007. Springer Handbook of Experimental Fluid Mechanics. Springer.

[24] Zhang, L. and Fox, M. 1999. Flat Plate Film Cooling Measurements using PSP Gas Chromatograph Techniques. Proc. Fifth ASME/JSME Joint Thermal Engineering Conference.

[25] Liu, T., Guille, M., and Sullivan, J. P., 2001. "Accuracy of Pressure-Sensitive Paint". AIAA Journal, 39(1), pp. 103–112.

[26] Han, J. and Rallabandi, A. 2010. Turbine Blade Film Cooling Using PSP Technique. Frontiers in Heat and Mass Transfer. Frontiers in Heat and Mass Transfer, 1 (DOI: 013001).

[27] Bauer, K., Grigull, U., and Straub, J. 1980. Influence of Free-stream Turbulence Intensity on Heat Transfer in the Two-Dimensional Turbulent Boundary Layer of an Accelerated Compressible Flow. Applied Thermal Engineering, 23. 10.1016/0017-9310.